

Sonic Anemometer as a Small Acoustic Tomography Array

Sergey N. Vecherin · Vladimir E. Ostashev · Christopher W. Fairall ·
D. Keith Wilson · Ludovic Bariteau

Received: 6 December 2012 / Accepted: 18 July 2013 / Published online: 6 August 2013
© Springer Science+Business Media Dordrecht 2013

Abstract The spatial resolution of a sonic anemometer is limited by the distance between its transducers, and for studies of small-scale turbulence and theories of turbulence, it is desirable to increase this spatial resolution. We here consider resolution improvements obtainable by treating the sonic anemometer as a small tomography array, with application of appropriate inverse algorithms for the reconstruction of temperature and velocity. A particular modification of the sonic anemometer is considered when the number of its transducers is doubled and the time-dependent stochastic inversion algorithm is used for reconstruction. Numerical simulations of the sonic anemometer and its suggested modification are implemented with the temperature and velocity fields modelled as discrete eddies moving through the sonic's volume. The tomographic approach is shown to provide better reconstructions of the temperature and velocity fields, with spatial resolution increased by as much as a factor of ten. The spatial resolution depends on the inverse algorithm and also improves by increasing the number of transducers.

Keywords Acoustic tomography · Small-scale turbulence · Sonic anemometer

1 Introduction

Sonic anemometers are robust instruments for measurements of temperature and velocity and have been used for such measurements for many decades, e.g., [Kaimal and Finnigan](#)

S. N. Vecherin · D. K. Wilson
U.S. Army Engineer Research and Development Center, 72 Lyme Road, Hanover, NH 0375, USA
e-mail: Sergey.N.Vecherin@erdc.dren.mil

V. E. Ostashev (✉) · L. Bariteau
Cooperative Institute for Research in Environmental Sciences, University of Colorado at Boulder,
325 Broadway, Boulder, CO 80305-3337, USA
e-mail: vladimir.ostashev@noaa.gov

C. W. Fairall
NOAA/Earth System Research Laboratory, 325 Broadway, Boulder, CO 80305-3337, USA

(1994). Due to concerns about flow distortion, the transducers of a sonic anemometer are located at some distance from each other, and as a result a sonic anemometer enables only path-averaged measurements of temperature and velocity. Horst and Oncley (2006) reviewed currently used sonic anemometers and showed theoretically that such an instrument enables the correct measurement of spectra up to a wavenumber that is about the inverse of the distance between its transducers. There are, however, several important applications/concerns in boundary-layer physics and turbulence theory that require analysis of turbulent fields at smaller scales (e.g., Fairall et al. 2003; Chamecki and Dias 2004). Among these are: (i) studies of the inertial subrange at small scales that are important for analysis of the dissipation rate and the turbulent kinetic energy budget, (ii) studies of turbulence closure models, (iii) studies of energy transfer in the atmospheric boundary layer that are important, for example, for wind energy applications, (iv) measurements of turbulence, particularly momentum and heat fluxes, when the energy-containing range extends to spatial scales smaller than those resolved by currently used sonic anemometers, e.g., near the surface or within canopies, (v) studies of small-scale turbulence for the Ameriflux CO₂ flux network. In principle, hot-wire and cold-wire anemometers enable one to make measurements of small-scale turbulence, but such anemometers are unreliable, often suffering mechanical break-down. Furthermore, they disturb the flow around them. Therefore, there is a need for a new generation of sonic anemometers/thermometers with increased spatial resolution. The main goal of the present paper is to study the feasibility of using a sonic anemometer as a small acoustic tomography array to increase the spatial resolution in measurements of temperature and velocity.

Ultrasound travel-time tomography has been used for many years in medicine and technology for reconstructing the image of a medium through which the ultrasound waves propagate. In these fields, the number of ultrasound propagation paths usually greatly exceeds the number of unknown parameters of the medium so that tomographic reconstruction is an overdetermined inverse problem.

The first experimental implementation of acoustic travel-time tomography of the atmospheric surface layer was reported by Wilson and Thomson (1994). In that case, the number of sound propagation paths is usually less than the number of temperature and wind velocity values to be reconstructed at selected points within the tomographic region, so that one deals with an underdetermined inverse problem. To solve this problem, the time-dependent stochastic inversion (TDSI) algorithm was recently developed and successfully applied to the reconstruction of the temperature T and wind velocity \mathbf{v} fields in acoustic tomography experiments (Vecherin et al. 2006, 2008). The current status of acoustic tomography of the atmospheric surface layer is reviewed in Ostashev et al. (2009).

Here, we suggest that one consider a sonic anemometer as a small acoustic tomography array and use appropriate inverse algorithms for reconstruction of the fine structure of the T and \mathbf{v} fields inside the sonic anemometer. A particular modification of the sonic anemometer is studied when the number of its transducers is doubled and the TDSI algorithm is used for tomographic reconstruction. Numerical simulations of temperature and velocity measurements with the sonic anemometer and its suggested modification are implemented. In the simulations, the T and \mathbf{v} fields inside the sonic anemometer and its modification are modelled with quasi-wavelets. The quasi-wavelets are eddy-like structures of temperature and velocity that are a convenient representation of turbulence at small scales (Wilson et al. 2009). The numerical simulations allow us to compare the errors in measurements of temperature and velocity with the sonic anemometer and its suggested modification, and the spatial resolutions with which the spectra of temperature and velocity fluctuations are obtained.

The paper is organized as follows. In Sect. 2, the geometry and principle of operation of the sonic anemometer and its suggested modification are considered. In Sect. 3, the results of numerical simulations are presented and discussed. Section 4 summarizes the results obtained in the paper.

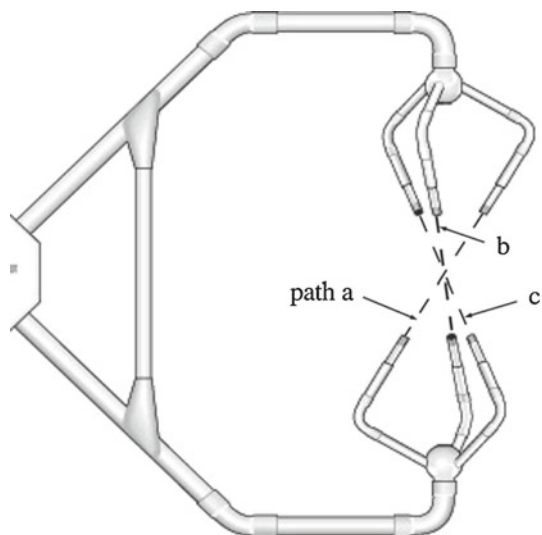
2 The Sonic Anemometer and Its Suggested Modification

2.1 Sonic Anemometer

Although the design of sonic anemometers varies substantially, their principle of operation is similar and can be understood by considering, for example, the CSAT3 sonic anemometer shown in Fig. 1. There are three transducers at both the “upper” and “lower” levels of the instrument that point downwards and upwards, respectively. In numerical simulations of the sonic anemometer, we assume that the upper and lower transducers are separated in the vertical direction by 0.2 m. These transducers form three sound propagation paths, marked as *a*, *b*, and *c*, whose elevation angles θ with respect to a horizontal plane are 60° . The projections of these paths on the horizontal plane located in the middle of the sonic anemometer intersect at 120° . The transducers serve alternately as sources (transmitters) and receivers. As a result, the sound pulses propagate in the opposite directions (i.e., upward and downward) of each path, thus enabling measurements of six travel times τ_i of sound propagation between transducers. Here, $i = 1, 2, \dots, N$, where $N = 6$.

A sonic anemometer enables measurements of the path-averaged values of the sound speed $c = \sqrt{\gamma_a R_a T}$ and the velocity $v = (v_x, v_y, v_z)$. Here, $\gamma_a = 1.40$ is the ratio of specific heats for dry air, $R_a = 287.058 \text{ J kg}^{-1} \text{ K}^{-1}$ is the specific gas constant for dry air, T is the acoustic virtual temperature, which, hereafter, is referred to as temperature, and v_x, v_y, v_z are the velocity components in a Cartesian coordinate system (x, y, z) . The sound speed c and, hence, the temperature T are determined from a sum of the travel times τ_i of sound propagation along the opposite directions of, e.g., the path *a*. The projections of the

Fig. 1 Schematic of the CSAT3 sonic anemometer. The ultrasound propagation paths *a*, *b*, and *c* are shown as dashed lines (reproduced from Horst and Oncley 2006)



velocity \mathbf{v} on the paths a , b , and c are determined from the differences of the travel times τ_i of sound propagation along the opposite directions of these paths, respectively. From these projections, it is straightforward to calculate v_x , v_y , and v_z . The corresponding relations can be found in Horst and Oncley (2006), and in the CSAT3 sonic anemometer instruction manual (1998). The spatial resolution of a sonic anemometer is determined by the length of the paths a , b , and c shown in Fig. 1.

2.2 A Sonic Anemometer as a Tomography Array

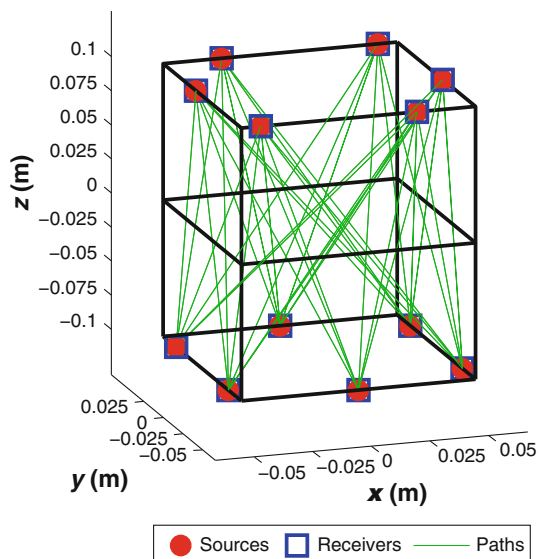
A suggested modification of the sonic anemometer is shown in Fig. 2. There are six transducers at both the upper and lower levels so that the number of transducers is doubled in comparison with a standard sonic anemometer. The lower- and upper-level transducers are located along the perimeter of a square with a side length of 0.1 m and are separated in the vertical direction by 0.2 m, i.e., the same distance as in the sonic anemometer considered above.

In Fig. 2, each transducer works alternately as a source and receiver. We also assume that each transducer at the lower level can receive signals from every transducer at the upper level, and vice versa. This increases the number of sound propagation paths to $6 \times 6 = 36$. Taking into account that sound signals can propagate in opposite directions of each path, the total number of travel times τ_i that can be measured with this modification of the sonic anemometer is $N = 72$.

2.3 Time-Dependent Stochastic Inversion

In the considered modification of the sonic anemometer, reconstruction of the temperature $T(\mathbf{R}, t)$ and velocity $\mathbf{v}(\mathbf{R}, t)$ fields is done with the TDSI algorithm, where $\mathbf{R} = (x, y, z)$ are the Cartesian coordinates and t is time. It is convenient to express these fields in the following form: $T(\mathbf{R}, t) = T_0(t) + T_1(\mathbf{R}, t)$ and $\mathbf{v}(\mathbf{R}, t) = \mathbf{v}_0(t) + \mathbf{v}_1(\mathbf{R}, t)$, where the subscripts “0” and “1” correspond to the mean fields (i.e., the fields averaged over the tomo-

Fig. 2 Schematic of the suggested modification of the sonic anemometer. Transducers at the upper ($z = 0.1$ m) and lower ($z = -0.1$ m) levels work alternately as ultrasound sources and receivers. Green lines are the ultrasound propagation paths between transducers



graphic volume) and their fluctuating parts, respectively. The mean fields $T_0(t)$ and $\mathbf{v}_0(t)$ are reconstructed from the measured travel times $\tau_i(t)$ using the least-square estimation. The temperature $T_1(\mathbf{R}, t)$ and velocity $\mathbf{v}_1(\mathbf{R}, t)$ fluctuations are reconstructed with the TDSI algorithm.

The main idea of the TDSI algorithm is to assume that the temperature and velocity fluctuations are random fields with the known spatial-temporal correlation functions $B_T(\mathbf{R}, t)$ and $B_{nm}(\mathbf{R}, t)$, respectively, where $n, m = 1, 2, 3$. The cross-correlation between temperature and velocity fluctuations is assumed to be zero, which is justified for small-scale turbulence. In TDSI, the travel times $\tau_i(t_j)$ are repeatedly measured at the time moments t_j , where $j = 1, 2, \dots, M$, and then used in the reconstruction of the temperature and velocity fluctuations at a specified time.

The input parameters in the least-square estimation of the mean fields, T_0 and \mathbf{v}_0 , and the TDSI algorithm for reconstruction of the fluctuations, T_1 and \mathbf{v}_1 , are the travel times $\tau_i(t_j)$ of sound propagation, the distances between transducers, and parameters of the spatial-temporal correlation functions $B_T(\mathbf{R}, t)$ and $B_{nm}(\mathbf{R}, t)$ (the latter two are needed for TDSI). The total fields $T(\mathbf{R}, t) = T_0(t) + T_1(\mathbf{R}, t)$ and $\mathbf{v}(\mathbf{R}, t) = \mathbf{v}_0(t) + \mathbf{v}_1(\mathbf{R}, t)$, and the estimated errors in their reconstruction, are calculated with equations derived in [Vecherin et al. \(2006\)](#).

Many numerical simulations of acoustic tomography of the atmosphere were implemented to test the TDSI algorithm. In the simulations, the temperature and velocity fields within a tomographic area or volume were modelled with large-eddy simulation (LES), e.g., [Sullivan et al. \(1994\)](#). Different forms of the correlation functions of temperature and velocity fluctuations were used: Gaussian, exponential, and the correlation functions, which correspond to the von Kármán spectra. The results showed that the accuracy of reconstruction depends insignificantly on the form of the correlation functions. Therefore, the Gaussian correlation functions are used herein, which enable some integrals in the TDSI inversion to be calculated analytically.

The Gaussian spatial-temporal correlation function of statistically homogeneous and stationary temperature fluctuations is given by ([Vecherin et al. 2006](#))

$$B_T(\mathbf{R}, t) = \sigma_T^2 \exp \left[-\frac{(\mathbf{R} - \mathbf{v}_0 t)^2}{L_T^2} \right], \quad (1)$$

where σ_T^2 is the variance of temperature fluctuations and L_T is the characteristic length. Equation 1 is obtained using Taylor's frozen-turbulence hypothesis. The spatial-temporal longitudinal correlation function of velocity fluctuations, $B_{RR}(\mathbf{R}, t)$, is given with this same equation if σ_T^2 and L_T are replaced with the variance σ_v^2 and the characteristic length L_v of velocity fluctuations, respectively. For homogeneous and isotropic turbulence, the spatial-temporal correlation functions $B_{nm}(\mathbf{R}, t)$ are expressed in terms of $B_{RR}(\mathbf{R}, t)$ with equations known in the literature (e.g., Eq. 6.34 in [Ostashev 1997](#)). The characteristic lengths L_T and L_v determine to an order of magnitude the smallest scales of temperature and velocity fluctuations that can be resolved in reconstruction. The larger scales of turbulence reconstructed with TDSI can be anisotropic and have correlation functions that differ from the Gaussian correlation functions. For example, numerical simulations showed that the TDSI algorithm enables accurate reconstruction of the LES fields corresponding to stable, neutral, and unstable stratifications ([Ostashev et al. 2009](#)). There is a trade-off between the values of L_T and L_v and the expected errors in the reconstruction of temperature and velocity fluctuations; the smaller are the L_T and L_v values the larger are the errors.

3 Numerical Simulations

3.1 Representation of Turbulence as Quasi-Wavelets

In numerical simulation, the temperature and velocity fields have been modelled as quasi-wavelets (Wilson et al. 2009). Since quasi-wavelets are not yet widely used in the literature, their properties are briefly reviewed below.

An individual temperature quasi-wavelet describes a fluctuation in temperature with respect to the mean temperature,

$$T_1^{\alpha n}(\mathbf{R}) = q^{\alpha n} f(|\mathbf{R} - \mathbf{b}^{\alpha n}|/l_\alpha), \quad (2)$$

where f is a spatially localized parent function (e.g., a Gaussian or exponential function), which is the same for all quasi-wavelets, $\mathbf{b}^{\alpha n}$ is the centre of the quasi-wavelet, l_α is its size, and $q^{\alpha n}$ is its amplitude. The index $\alpha = 1, 2, \dots, N$ corresponds to the size of a quasi-wavelet, with l_1 being the largest size and l_N the smallest; the index $n = 1, 2, \dots, N_\alpha$ describes different quasi-wavelets with the same size l_α . The sum of quasi-wavelets gives us the field of the temperature fluctuations $T_1(\mathbf{R})$. To construct an ensemble of quasi-wavelets, it is assumed that the centres $\mathbf{b}^{\alpha n}$ are randomly located in the considered volume, the mean value of the amplitude $q^{\alpha n}$ is zero, and the second moment is given by $\langle q^{\alpha n} q^{\beta m} \rangle = \delta_{\alpha\beta} \delta_{nm} q_\alpha^2$, where δ_{nm} is the Kronecker delta and q_α^2 is the mean squared amplitude. The remainder of the parameters in Eq. 2 are deterministic and the ratio $l_{\alpha+1}/l_\alpha = e^{-\mu}$ is assumed constant. The volume occupied by the quasi-wavelets with the size l_α is $V_\alpha = N_\alpha l_\alpha^3$. The spatial spectrum of an ensemble of quasi-wavelets depends on the form of a parent function, parameter μ , and the dependence of q_α and V_α on α . With these choices, realistic spectra of temperature fluctuations can be obtained, such as the Kolmogorov and von Kármán spectra.

Velocity quasi-wavelets are constructed similarly (Wilson et al. 2009). Thus, quasi-wavelets are similar to wavelets in that they are based on translations and dilations of a parent function; however, their positions are random. Quasi-wavelets enable the modelling of intermittent, inhomogeneous, and anisotropic turbulence with prescribed statistical properties. One of the applications of quasi-wavelets is to generate the temperature and velocity fields needed in numerical simulations of sound propagation through a turbulent atmosphere.

In this paper, quasi-wavelets were used to generate statistically homogeneous and isotropic temperature and velocity fluctuations inside the sonic anemometer volume and its suggested modification. The smallest and largest quasi-wavelets were chosen as $l_1 = 0.01$ m and $l_N = 2$ m, respectively, while other parameters of the quasi-wavelets were chosen to ensure realistic power spectra of temperature and velocity fluctuations.

In numerical simulation, the size of the computational grid along the x , y , and z -axes is equal to the smallest quasi-wavelet, i.e., 0.01 m. The quasi-wavelet temperature and velocity fields were created in a volume of $20 \text{ m} \times 0.1 \text{ m} \times 0.2 \text{ m}$; in the simulations, this volume moved in the direction of the x -axis with velocity $U = 2 \text{ m s}^{-1}$; the total time of the numerical experiment was $(20 \text{ m})/(2 \text{ m s}^{-1}) = 10$ s. Figure 3 shows a snapshot of the temperature and three components of the velocity fields inside the sonic anemometer and its suggested modification obtained with quasi-wavelets. In the numerical simulations, the discretization time was 0.005 s so that the total number of snapshots of the T and \mathbf{v} fields was 2000. For each snapshot, the travel times τ_i along all sound propagation paths in the sonic anemometer (Fig. 1) and its suggested modification (Fig. 2) were calculated.

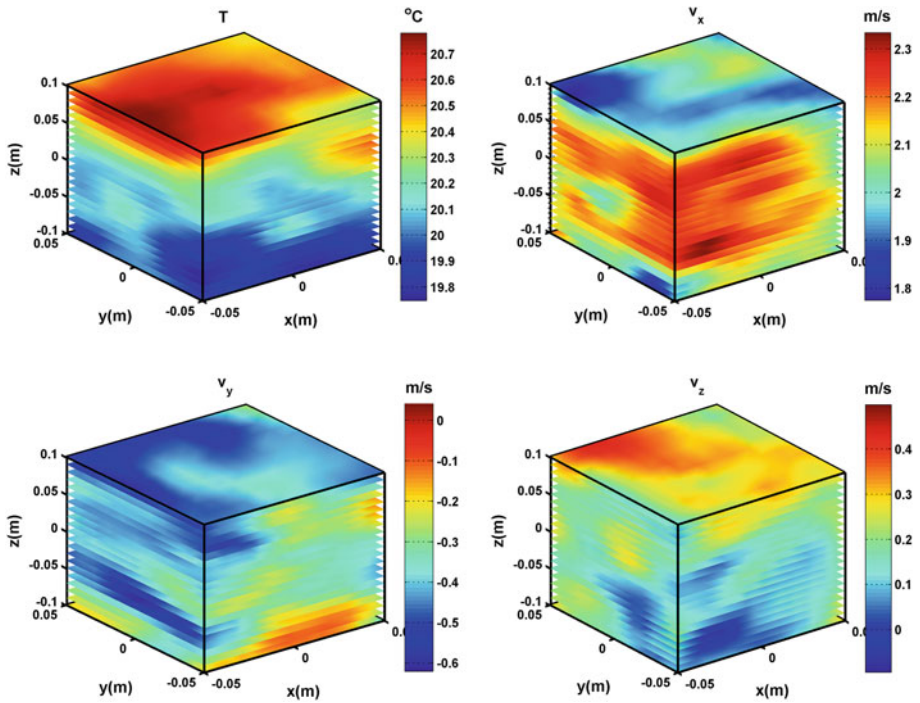


Fig. 3 Snapshot of the temperature and three components of the velocity fields obtained with quasi-wavelets. Upper left: $T(x, y, z)$, upper right: $v_x(x, y, z)$, lower left: $v_y(x, y, z)$, and lower right: $v_z(x, y, z)$

3.2 Reconstruction of Temperature and Velocity Fields

The travel times τ_i for the sonic anemometer were, then, used to calculate the path-averaged values of temperature and velocity with equations known in the literature (e.g., Kaimal and Finnigan 1994). The obtained time series of $T, v_x, v_y,$ and v_z are depicted as red lines in the left-hand plots in Figs. 4, 5, 6 and 7, respectively; the blue lines are the quasi-wavelet values of $T, v_x, v_y,$ and v_z at the centre of the sonic anemometer. The agreement between these quasi-wavelet values and the path-averaged values of $T, v_x, v_y,$ and v_z reconstructed in numerical simulations of the sonic anemometer is relatively good. This comparison shows to what extent the path-averaged values of temperature and velocity represent the corresponding values at the centre of a sonic anemometer. The root-mean-square errors (*RMSEs*) between the red and blue lines in the left plots in Figs. 4–7 are $\sigma_T^s = 0.09 \text{ }^\circ\text{C}, \sigma_{v_x}^s = 0.086 \text{ m s}^{-1}, \sigma_{v_y}^s = 0.083 \text{ m s}^{-1},$ and $\sigma_{v_z}^s = 0.056 \text{ m s}^{-1},$ respectively, where the superscript “s” stands for “sonic”. The *RMSE* for the vertical velocity, $\sigma_{v_z}^s,$ is about 1.5 times smaller than the *RMSE* for the horizontal components of the velocity, $\sigma_{v_x}^s$ and $\sigma_{v_y}^s,$ and is due to the fact that the sound propagation paths in the sonic anemometer have relatively large elevation angles $\theta = 60^\circ.$ Indeed, using equations known in the literature, e.g., Eqs. 9a–9c in Horst and Oncley (2006), v_x, v_y, v_z are calculated from the velocity components v_a, v_b, v_c measured with the sonic anemometer along the sound propagation paths a, b, c shown in Fig. 1. If Δv is the error in the measurement of $v_a, v_b, v_c,$ it follows from these equations that the error in the measurement of v_x or v_y is proportional to $\Delta v / \cos \theta,$ while the error in the measurement of v_z is proportional to $\Delta v / \sin \theta.$ For $\theta = 60^\circ,$ the former error is larger than the latter by

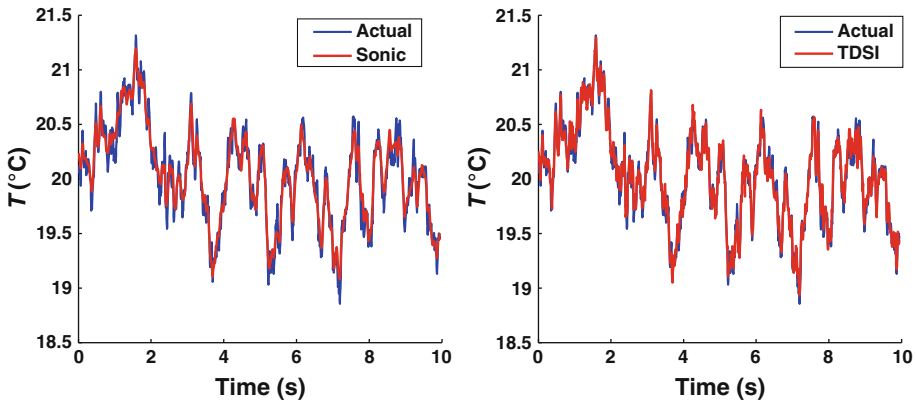


Fig. 4 Time series of temperature, $T(t)$. Blue lines are the quasi-wavelet values of temperature at the centre of the sonic anemometer and its suggested modification. Red lines are the values of temperature reconstructed in numerical simulations of the sonic (left plot) and its modification (right plot)

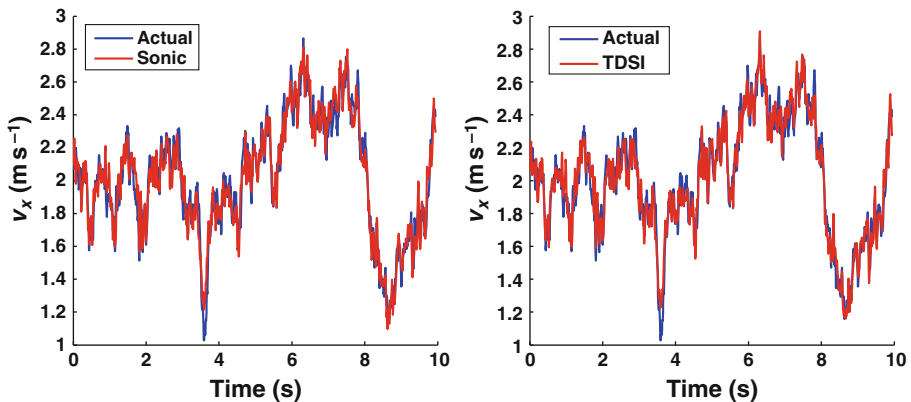


Fig. 5 Time series of the x -component of the horizontal velocity, $v_x(t)$. Blue lines are the quasi-wavelet values of v_x at the centre of the sonic anemometer and its suggested modification. Red lines are the values of v_x reconstructed in numerical simulations of the sonic (left plot) and its modification (right plot)

$\tan 60^\circ \approx 1.73$, which is close to the ratios $\sigma_{v_x}^s / \sigma_{v_z}^s = 1.54$ and $\sigma_{v_y}^s / \sigma_{v_z}^s = 1.48$ obtained in numerical simulations.

Then, the travel times τ_i for the considered modification of the sonic anemometer were used as input parameters for reconstruction of the mean and fluctuating parts of the temperature and velocity fields. In the TDSI algorithm for reconstruction of the fluctuations, three consecutive values of the travel times τ_i were employed. Furthermore, the square roots of the variances of the spatial-temporal correlation functions of temperature and the three components of velocity fluctuations were calculated for the considered quasi-wavelet field, and were 0.074°C , 0.057 m s^{-1} , 0.058 m s^{-1} , and 0.064 m s^{-1} , respectively; the characteristic length of these fluctuations was $L_T = L_v = 0.03 \text{ m}$. In the right-hand plots in Figs. 4–7, the time series of the reconstructed values of T , v_x , v_y , and v_z in the centre of the considered modification of the sonic anemometer are shown as red lines, respectively. The blue lines are again the quasi-wavelet values of T , v_x , v_y , and v_z in the centre of the sonic anemometer, i.e., the blue lines in the left-hand and right-hand plots in these figures are the

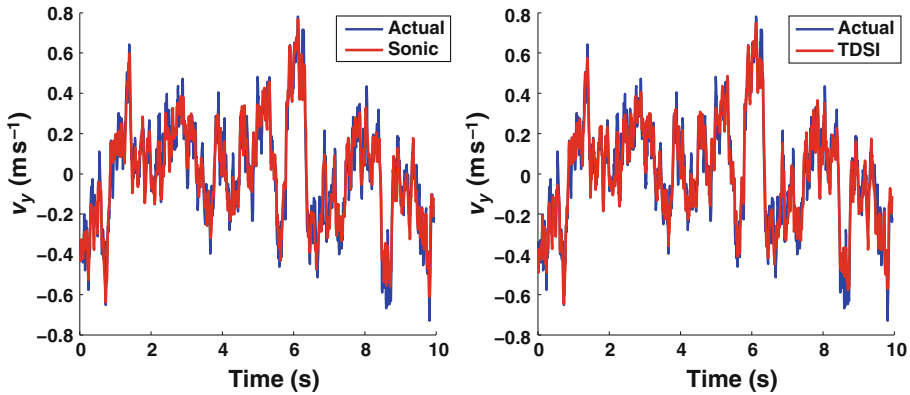


Fig. 6 Time series of the y -component of the horizontal velocity, $v_y(t)$. *Blue lines* are the quasi-wavelet values of v_y at the centre of the sonic anemometer and its suggested modification. *Red lines* are the values of v_y reconstructed in numerical simulations of the sonic (*left plot*) and its modification (*right plot*)

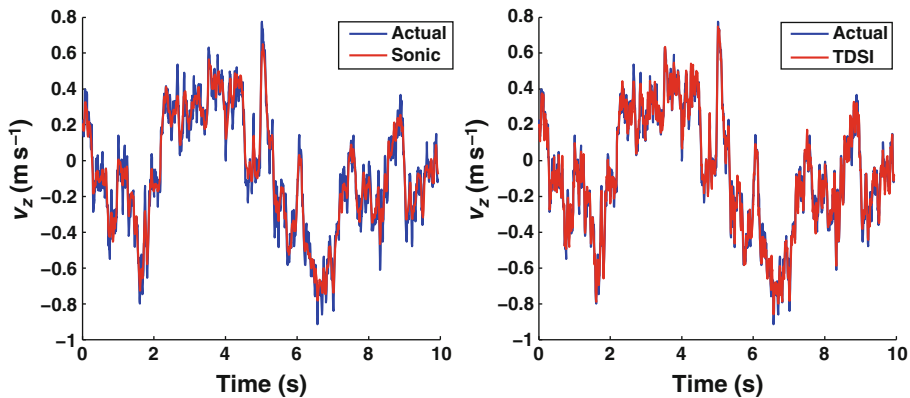


Fig. 7 Time series of the vertical component of the velocity, $v_z(t)$. *Blue lines* are the quasi-wavelet values of v_z at the centre of the sonic anemometer and its suggested modification. *Red lines* are the values of v_z reconstructed in numerical simulations of the sonic (*left plot*) and its modification (*right plot*)

same. It follows from the right-hand plots in Figs. 4–7 that the agreement between the quasi-wavelet and reconstructed values of T , v_x , v_y , and v_z is very good, and, in fact, is better than for the sonic anemometer (see left-hand plots). The *RMSEs* between the quasi-wavelet and reconstructed values of T , v_z , v_x , and v_y are smaller than those for the sonic anemometer: $\sigma_T^m = 0.75\sigma_T^s = 0.067\text{ }^\circ\text{C}$, $\sigma_{v_x}^m = 0.91\sigma_{v_x}^s = 0.077\text{ m s}^{-1}$, $\sigma_{v_y}^m = 0.85\sigma_{v_y}^s = 0.07\text{ m s}^{-1}$, and $\sigma_{v_z}^m = 0.62\sigma_{v_z}^s = 0.035\text{ m s}^{-1}$, respectively. Here, the superscript “m” stands for the modification of the sonic anemometer.

The results of the numerical simulations shown in Figs. 4–7 clearly indicate that the suggested modification of the sonic anemometer enables a more accurate reconstruction of the temperature and vertical velocity, and somewhat better reconstruction of the horizontal velocity. These results are used in the next sub-section to study the reconstruction of the spectra of temperature and velocity fluctuations with the sonic anemometer and its modification. Note that the TDSI algorithm was also applied to the reconstruction of temperature and velocity fields inside the sonic anemometer (Fig. 1). Though not presented here for brevity, the results

obtained showed no significant improvement in the reconstruction of temperature and the three components of the velocity in comparison with their path-averaged values.

3.3 Spectra of Temperature and Velocity Fluctuations

The time series T , v_x , v_y , and v_z obtained in numerical simulations of the sonic anemometer and its suggested modification and the corresponding values of the quasi-wavelets in the centre of the sonic were employed to calculate the mean values of temperature and three components of the velocity and their fluctuating parts. The fluctuations were then used to calculate the power spectra $S_j^s(k)$, $S_j^m(k)$, and $S_j^{qw}(k)$, where “s” stands for the sonic, “m” for its suggested modification, “qw” for quasi-wavelets, and k is the turbulence wavenumber. The subscript j stands for T , x , y , or z and corresponds to fluctuations in temperature or the three components of the velocity.

The spectral transfer functions are defined as the ratios of the power spectra (e.g., Horst and Oncley 2006; Angelou et al. 2012), viz.

$$H_j^s(k) = \frac{S_j^s(k)}{S_j^{qw}(k)}, \quad (3a)$$

$$H_j^m(k) = \frac{S_j^m(k)}{S_j^{qw}(k)}. \quad (3b)$$

The spectral transfer functions characterize the effects of path averaging and errors in reconstruction of the power spectra of temperature and velocity fluctuations obtained in numerical simulations of the sonic anemometer and its suggested modification. The spectral transfer functions are plotted in Fig. 8; the red and blue lines correspond to $H_j^s(k)$ and $H_j^m(k)$, respectively. For a perfect reconstruction of the spectra, these lines would coincide with the black horizontal lines corresponding to the case $H_j^s(k) = H_j^m(k) = 1$.

It follows from the upper left-hand and lower right-hand plots in Fig. 8 that the sonic anemometer enables the correct reconstruction of both the temperature and vertical velocity spectra for the wavenumbers k smaller than about $k_{ps}^s = 10 \text{ m}^{-1}$, where “ps” stands for the power spectrum. Let us compare k_{ps}^s with a similar value obtained by Horst and Oncley (2006) who studied analytically the effect of path averaging in the CSAT3 sonic anemometer. It follows from Fig. 3 in that paper that the spectral transfer functions $H_j^s(k)$ are close to 1 for k smaller than about $k_0^s = 1/L$, where L is the distance between the transducers. In the sonic anemometer considered herein, $L = 0.23 \text{ m}$ so that $k_0^s = 4.3 \text{ m}^{-1}$. The difference between k_0^s and k_{ps}^s can be explained by the variability in the red (and blue) curves in Fig. 8, which is due to the errors in reconstruction and which makes it difficult to determine the exact value of the cut-off frequency k_{ps}^s . It also follows from the upper left-hand and lower right-hand plots in Fig. 8 that the suggested modification of the sonic anemometer enables the correct reconstruction of the temperature and vertical velocity spectra for k smaller than about $k_{ps}^m = 100 \text{ rad m}^{-1}$, thus increasing its spatial resolution by a factor of $k_{ps}^m/k_{ps}^s = 10$.

The spectral transfer functions for the horizontal velocity components, v_x and v_y , reconstructed in numerical simulations of the sonic anemometer and its modification are shown in the upper right-hand and lower left-hand plots in Fig. 8, respectively. It follows from these figures that the spectral transfer functions significantly deviate from 1 in the range $k \gtrsim 10 \text{ m}^{-1}$ and that the reconstruction accuracy is about the same for the sonic anemometer and its modification. These results are due to predominantly vertical orientations of the sound propagation paths for both the sonic anemometer and its modification, when the horizontal components of the velocity are reconstructed less accurately than the vertical component.

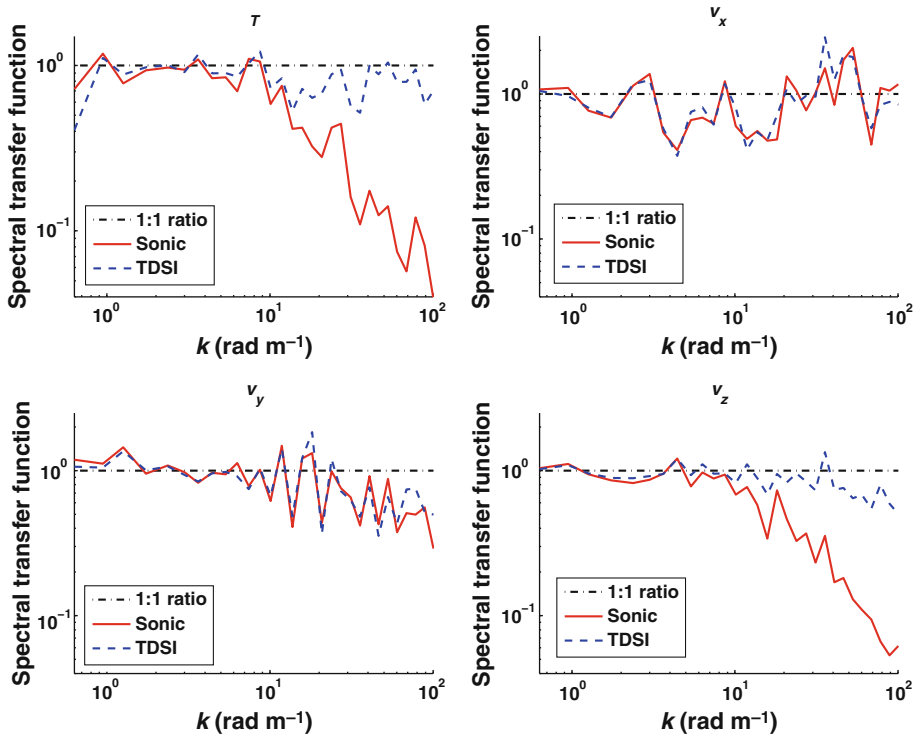


Fig. 8 Spectral transfer functions defined through the power spectra and obtained in numerical simulations of the sonic anemometer ($H_j^s(k)$, red lines) and its suggested modification ($H_j^m(k)$, blue lines). The black, horizontal lines correspond to the case $H_j^s(k) = H_j^m(k) = 1$. Upper left T fluctuations; upper right v_x fluctuations; lower left v_y fluctuations; and lower right v_z fluctuations

Figure 8 also shows that the fastest decrease of the spectral transfer functions obtained in numerical simulations of the sonic anemometer is for the temperature power spectrum, followed by the power spectra of v_z , v_y , and v_x . The spectral transfer functions plotted in Fig. 3 in Horst and Oncley (2006) have qualitatively the same behaviour.

Angelou et al. (2012) argue that the effect of path averaging on measurements of the radial component of the wind velocity with a laser anemometer should be taken into account using cross-spectra rather than power spectra. Indeed, the noise in the experimental data can be amplified in the power spectrum, while it is cancelled in the cross-spectrum. In the present paper, the noise in the data is due to the errors in numerical reconstruction of the temperature and velocity fields. As a result, the spectral transfer functions in Fig. 8 have noticeable variability and are >1 for some values of k though they should always be ≤ 1 .

Following Angelou et al. (2012), the cross-spectra $\chi_j^{s,qw}(k)$ between fluctuations in temperature or velocity components obtained in numerical simulations of the sonic anemometer and the corresponding values of the quasi-wavelets in the centre of the sonic were calculated. Similarly, the cross-spectra $\chi_j^{m,qw}(k)$ between fluctuations in temperature or velocity components obtained in numerical simulations of the suggested modification of the sonic anemometer and the values of the quasi-wavelets were also calculated. The spectral transfer functions are now defined similarly to those in Angelou et al. (2012),

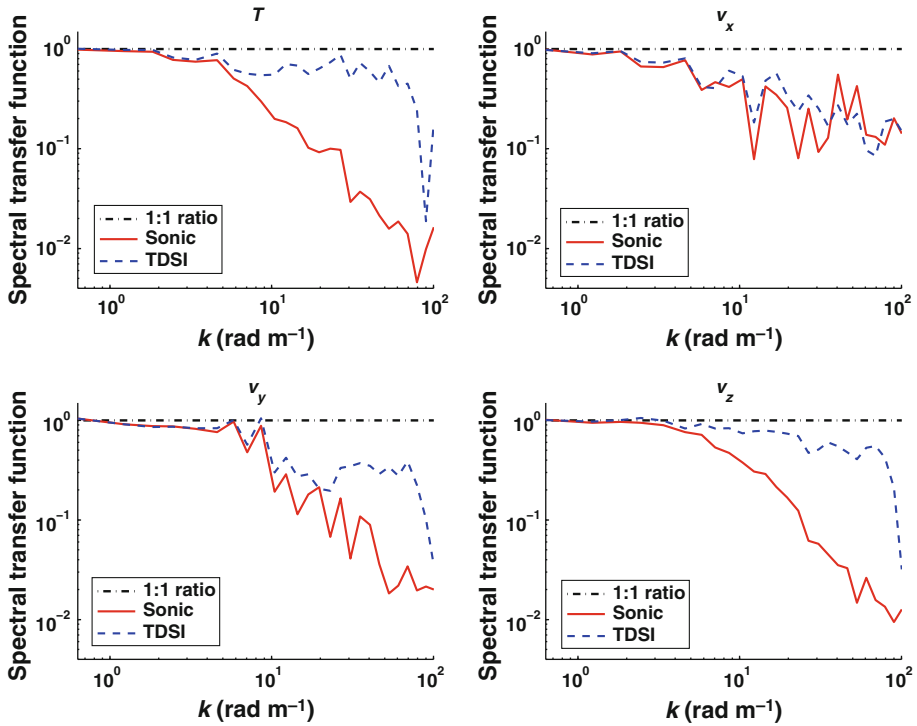


Fig. 9 Spectral transfer functions defined through the cross-spectra and obtained in numerical simulations of the sonic anemometer ($h_j^s(k)$, red lines) and its suggested modification ($h_j^m(k)$, blue lines). The black, horizontal lines correspond to the case $h_j^s(k) = h_j^m(k) = 1$. Upper left T fluctuations; upper right v_x fluctuations; lower left v_y fluctuations; and lower right v_z fluctuations

$$h_j^s(k) = \frac{(\text{Re } \chi_j^{s,qw}(k))^2}{(S_j^{qw}(k))^2}, \tag{4a}$$

$$h_j^m(k) = \frac{(\text{Re } \chi_j^{m,qw}(k))^2}{(S_j^{qw}(k))^2}. \tag{4b}$$

The spectral transfer functions $h_j^s(k)$ and $h_j^m(k)$ are plotted in Fig. 9; the red and blue lines correspond to $h_j^s(k)$ and $h_j^m(k)$, respectively; the black horizontal lines to the case $h_j^s(k) = h_j^m(k) = 1$.

The spectral transfer functions in Fig. 9 confirm conclusions made from Fig. 8: the suggested modification of the sonic anemometer enables us to increase the spatial resolution of the temperature and vertical velocity, while the spatial resolution of the horizontal velocity remains approximately unchanged. These results are actually more evident in Fig. 9 since the cross-spectra in the upper left-hand and lower right-hand plots in Fig. 9 have less variability than similar power spectra in Fig. 8. Furthermore, the spectral transfer functions in Fig. 9 are ≤ 1 , as they should be. It follows from the upper left-hand and lower right-hand plots in this figure that the sonic anemometer enables the correct reconstruction of both the temperature

and vertical velocity spectra for wavenumber k smaller than about $k_{cs}^s = 5 \text{ m}^{-1}$, where the subscript “cs” stands for cross-spectra. This value of k_{cs}^s is close to $k_0^s = 4.3 \text{ m}^{-1}$ obtained from the analytical analysis. Furthermore, it follows from these plots that the spectral transfer functions for temperature and vertical velocity obtained in numerical simulations of the suggested modification of the sonic anemometer are close to 1 for $k \lesssim 50 \text{ m}^{-1}$. Thus, the sonic anemometer as a small tomography array enables us to increase the spatial resolution by a factor of about $50/5 = 10$. For $k \gtrsim 80 \text{ m}^{-1}$, the spectral transfer functions in Fig. 9 increase or oscillate due to numerical instability caused by small values of the power spectra and cross-spectra at such wavenumbers.

4 Conclusions

To increase the spatial resolution of a sonic anemometer, it is suggested that one consider it as a small acoustic tomography array and apply appropriate inverse methods for reconstruction of the temperature and velocity fields. A particular modification of the sonic anemometer was studied when the number of its transducers is doubled and reconstruction of the temperature and velocity fields is done with the TDSI algorithm. Numerical simulations of the sonic anemometer and its suggested modification were implemented with the temperature and velocity fields modelled as quasi-wavelets. The simulations showed that the sonic anemometer enables measurements of the time series of temperature and velocity with a relatively small root-mean-square error (*RMSE*). The suggested modification of the sonic anemometer allows even more accurate measurements, especially for temperature and the vertical component of velocity, when the corresponding *RMSE* is smaller than that for the sonic anemometer by factors 0.75 and 0.62, respectively. The increase in accuracy is less pronounced for the horizontal components of velocity due to the predominantly vertical orientations of the ultrasound propagation paths in the sonic anemometer and its modification.

Another advantage of the considered modification of the sonic anemometer is a significant increase in the spatial resolution of the spectra of temperature and vertical velocity fluctuations. The numerical simulations showed that the sonic anemometer enables correct measurements of these spectra up to wavenumbers, that is about the inverse of the distance between its transducers. This result clearly indicates the effect of path averaging on the measurements of the spectra and agrees with that obtained by Horst and Oncley (2006) who used an analytical approach. On the other hand, the considered modification of the sonic anemometer enables correct reconstruction of these spectra up to the wavenumbers that are about ten times larger than those for the sonic anemometer. Its spatial resolution, generally, depends on the inverse algorithm for reconstruction of the temperature and velocity fields and also improves by increasing the number of transducers.

From a technological point of view, the considered modification of the sonic anemometer seems feasible; other modifications might also be feasible with more transducers at the upper and lower levels. With the increased number of transducers, the spatial resolution can be increased further. Also, the inverse problem in the reconstruction of temperature and velocity might become overdetermined so that standard inverse algorithms (e.g., the least-square estimation) can be employed. Note that the increased number of transducers might increase the flow distortion. However, the distance between transducers can be increased so that the temperature and velocity fields in the centre of a sonic volume will not be distorted and can be reconstructed with the use of acoustic tomography. Since acoustic tomography provides turbulent fields at all points inside a sonic anemometer, it can also be used to study the flow distortion caused by transducers.

Acknowledgements This material is based upon work supported in part by the U. S. Army Research Laboratory and the U. S. Army Research Office under contract/grant number W911NF1010415 to Dr. Ostashev. Permission to publish was granted by Director, Cold Regions Research and Engineering Laboratory. We would like to thank two anonymous reviewers whose comments allowed us to improve the paper.

References

- Angelou N, Mann J, Sjöholm M, Courtney M (2012) Direct measurement of the spectral transfer function of a laser based anemometer. *Rev Sci Instrum* 83:033111, 7 pp
- Chamecki M, Dias NL (2004) The local isotropy hypothesis and the turbulent kinetic energy dissipation rate in the atmospheric surface layer. *Q J R Meteorol Soc* 130:2733–2752
- CSAT3 (1998) Three dimensional sonic anemometer instruction manual. Campbell Scientific Inc., Logan, 14 pp
- Fairall CW, Bradley EF, Hare JE, Grachev AA, Edson JB (2003) Bulk parametrization of air–sea fluxes: updates and verification of the COARE algorithm. *J Clim* 16:571–591
- Horst TW, Oncley SP (2006) Corrections to inertial-range power spectra measured by CSAT3 and solent sonic anemometers, 1. Path-averaging errors. *Boundary-Layer Meteorol* 119:375–395
- Kaimal JC, Finnigan JJ (1994) Atmospheric boundary layer flows: their structure and measurement. Oxford University Press, Oxford, 304 pp
- Ostashev VE (1997) Acoustics in moving inhomogeneous media. E & FN SPON, London 259 pp
- Ostashev VE, Vecherin SN, Wilson DK, Ziemann A, Goedecke GH (2009) Recent progress in acoustic travel-time tomography of the atmospheric surface layer. *Meteorol Zeitschrift* 18:125–133
- Sullivan PP, McWilliams JC, Moeng C-H (1994) A subgrid-scale model for large-eddy simulation of planetary boundary-layer flows. *Boundary-Layer Meteorol* 71:247–276
- Vecherin SN, Ostashev VE, Goedecke GH, Wilson DK, Voronovich AG (2006) Time-dependent stochastic inversion in acoustic travel-time tomography of the atmosphere. *J Acoust Soc Am* 119:2579–2588
- Vecherin SN, Ostashev VE, Wilson DK, Ziemann A (2008) Time-dependent stochastic inversion in acoustic tomography of the atmosphere with reciprocal transmission. *Meas Sci Technol* 19:125501–125512
- Wilson DK, Thomson DW (1994) Acoustic tomographic monitoring of the atmospheric surface layer. *J Atmos Ocean Technol* 11:751–769
- Wilson DK, Ostashev VE, Goedecke GH (2009) Quasi-wavelet formulations of turbulence and other random fields with correlated properties. *Probab Eng Mech* 24:343–357